51. Shemesh N, Ozarslan E, Basser PJ, Cohen Y (2009) Measuring small compartmental dimensions with low-q angular double-PGSE NMR: The effect of experimental parameters on signal decay. Journal of Magnetic Resonance 198: 15–23.
52. Kunimatsu A, Aoki S, Masutani Y, Abe O, Mori H, et al. (2003) Three-dimensional white matter tractography by diffusion tensor imaging in ischaemic stroke involving the corticospinal tract. Neuroradiology 45: 532–535.
53. Yamada K, Kizu O, Kubota T, Ito H, Matsushima S, et al. (2007) The pyramidal tract has a predictable course through the centrum semiovale: a diffusion-tensor based tractography study. Journal of Magnetic Resonance Imaging 26: 519–524.
54. Barazany D, Jones D, Assaf Y (2011) AxCaliber 3D. Proc Int Soc Magn Reson Med 19: 76.

JOURNAL OF MAGNETIC RESONANCE IMAGING 40:1208–1214 (2014)

Original Research

Non-Gaussian Diffusion-Weighted Imaging for Assessing Diurnal Changes in Intervertebral Disc Microstructure

Masaki Katsura, MD, PhD,[1]* Yuichi Suzuki, PhD,[2] Junichi Hata, PhD,[2] Masaaki Hori, MD, PhD,[3] Hiroki Sasaki, MD, PhD,[1] Hiroyuki Akai, MD, PhD,[1] Harushi Mori, MD,[1] Akira Kunimatsu, MD, PhD,[1] Yoshitaka Masutani, PhD,[1] Shigeki Aoki, MD, PhD,[3] and Kuni Ohtomo, MD, PhD[1]

Purpose: To investigate the use of non-Gaussian diffusion-weighted imaging (q-space imaging [QSI]) to estimate diurnal changes in intervertebral disc (IVD) microstructure.

Materials and Methods: IVDs of 15 male subjects (mean age, 27.3 years; mean body mass index, 22.50 kg/m^2) were investigated once in the morning, less than 30 min after rising, and a second time in the evening after at least 10 h of normal physical activity, using 3 Tesla (T) MR imaging. T2 mapping and QSI data values (apparent diffusion coefficient [ADC], root mean square displacement [RMSD], and apparent kurtosis coefficient [AKC]) were calculated and compared between the morning and evening imaging sessions.

Results: The T2, ADC, and RMSD values showed a significant decrease in the evening (175.8 ± 49.5 ms, 1.56 ± 0.32 10^{-3}mm^2/s and 40.0 ± 3.0 μm, respectively; $P < 0.05$ for all values; paired t-test), when compared with the morning values (226.5 ± 83.8 ms, 1.69 ± 0.29 10^{-3}mm^2/s and 45.2 ± 2.9 μm, respectively). The AKC value showed a significant increase in the evening (0.67 ± 0.08), when compared with the morning value (0.58 ± 0.04; $P < 0.05$).

Conclusion: The RMSD and AKC values obtained from QSI analysis may be biomarkers for IVD diurnal microstructural changes.

Key Words: non-Gaussian diffusion-weighted imaging; q-space imaging; intervertebral disc; diurnal changes
J. Magn. Reson. Imaging 2014;40:1208–1214.

THE INTERVERTEBRAL DISC (IVD) consists of the nucleus pulposus (NP) in the core and the annulus fibrosus (AF) at the periphery. The NP is rich in proteoglycans. Proteoglycans interact with hyaluronic acid to form proteoglycan aggregates that are negatively charged and hydrophilic, and which are designed to draw and retain water (1). The AF is composed predominantly of type I collagen organized in dense concentric lamellae forming a fibrous collagen network that maintains the shape of the disc (2).

It has been reported that the spine becomes shorter during the day and recovers during the night (3). This phenomenon has been thought to result from a decrease in disc hydration with daily compression (4). This hypothesis has been supported by several investigators studying morphological aspects of the IVDs, which function to distribute hydraulic pressure under compressive loads (5,6).

Several studies have identified diurnal IVD changes in vivo using magnetic resonance (MR) imaging. Previous investigators reported a decrease in IVD volume (7), and a decrease in NP T2 values (8,9) after a diurnal workload. In addition to morphologic MR imaging, diffusion-weighted imaging (DWI) has also been applied to measure IVD diurnal changes of molecular water diffusion as the apparent diffusion coefficient (ADC) (9). DWI is expected to reflect a microscopic restriction of water molecules and, thereby, microstructural changes such as matrix composition (water, proteoglycan, and collagen) and matrix integrity (9–11).

Conventional DWI analysis is based on an assumption that the water molecules follow a Gaussian distribution. However, human tissue including the IVD is a complex and restricted environment that hinders the

[1]Department of Radiology, Graduate School of Medicine, The University of Tokyo, Tokyo, Japan.
[2]Department of Radiological Technology, The University of Tokyo Hospital, Tokyo, Japan.
[3]Department of Radiology, School of Medicine, Juntendo University, Tokyo, Japan.
Presented in part at the 21st Annual Meeting of the International Society of Magnetic Resonance in Medicine, April 20–26, 2013, Salt Lake City, USA.
*Address reprint requests to: M.K., Department of Radiology, Graduate School of Medicine, The University of Tokyo, 7-3-1 Hongo, Bunkyo-ku, Tokyo 113–8655, Japan.
E-mail: mkatsura-tky@umin.ac.jp
Received October 8, 2012; Accepted September 11, 2013.
DOI 10.1002/jmri.24459
View this article online at wileyonlinelibrary.com.

Table 1.
Morning and Evening T2 Values*

	Morning	Evening	*P* value
ROI 1	67.6 ± 10.5	74.0 ± 14.5	0.08
ROI 2	160.2 ± 53.4	157.0 ± 55.6	0.81
ROI 3	226.5 ± 83.8	175.8 ± 49.5	< 0.01*
ROI 4	146.8 ± 51.9	144.1 ± 49.4	0.69
ROI 5	52.8 ± 7.9	49.9 ± 7.2	0.18

Shown are the results of the T2 value (ms) paired t-test analysis separated for region-of-interest localization. Data are displayed as the mean ± standard deviation. There was a significant decrease in the T2 value in the middle of the nucleus pulposus (ROI 3) in the evening (< 0.05). No significant differences between the morning and the evening were observed in other areas.

distribution of water molecules, resulting in distributions that are far from Gaussian (12). Diffusion signal decay is affected by numerous factors such as water restriction and intra- and extracellular water exchange, as well as variation in tissue compartment sizes. Therefore, different approaches that do not rely on the previously mentioned assumption are required to address all of the factors affecting the signal in diffusion-weighted sequences.

Q-space imaging (QSI) analysis is a more advanced form of diffusion analysis and uses a different approach to measure water molecule diffusion (13,14). In contrast to conventional DWI, QSI does not assume a Gaussian shape for the underlying probability density function (PDF) of water molecule diffusion. It has shown promise for evaluating the microstructure of tissues in vivo (15–18) because it can provide additional diffusion metrics, namely the root mean square displacement (RMSD) and apparent kurtosis coefficient (AKC) (19–22), which give in vivo microstructural information that complements the ADC values. For example, increased ADC can indicate either decreased viscosity of the tissue or spatial dilatation of the water movement space (23). It is difficult to distinguish between these phenomena when using ADC values only. However, the RMSD values reflect the real extent of water molecule movement (13,14). We, therefore, hypothesized that QSI analysis would be able to provide information about IVD diurnal microstructural changes beyond that provided by conventional DWI metrics based on an assumption of a Gaussian shape and model of water molecules.

The purpose of this study is to investigate the use of RMSD and AKC metrics of QSI data to estimate IVD composition diurnal changes.

MATERIALS AND METHODS

Subjects

We investigated 15 male subjects between the ages of 25 and 39 years (mean, 27.3), with a body mass index ranging from 20.06 to 25.56 kg/m^2 (mean, 22.50). We obtained institutional review board ethics approval before initiating the study. All subjects gave written informed consent. Subjects were included if they had no episodes of lower back or radicular pain in the last 6 months. None of the subjects had previous spine surgery, contraindications for MRI, or any previously diagnosed abnormalities of the lumbar spine. They were investigated once in the morning less than 30 min after rising and a second time in the evening after at least 10 h of normal physical activity (office work).

Image Acquisition

All images were acquired using 3 Tesla (T) MR (Signa HDx ver. 14.0; General Electric, Waukesha, WI). After fast spin-echo (FSE) T2-weighted sagittal and axial imaging, QSI and T2 mapping data were acquired in the axial plane of the IVD between the fourth and fifth lumbar vertebrae (L4/5 disc).

FSE T2-weighted images were acquired according to our routine protocol for clinical spine MRI. Imaging parameters for FSE T2-weighted sagittal images were as follows: repetition time (TR): 2740 [ms]; echo time (TE): 106.6 [ms]; number of excitations (NEX): 1.5; field of view (FOV): 28 [cm]; matrix size: 512 × 256; and slice thickness: 3.0 [mm]; imaging time approximately 2.5 min. Imaging parameters for FSE T2-weighted axial images were as follows: TR: 5000 [ms]; TE: 105.1 [ms]; NEX: 0.5; FOV: 25.6 [cm]; matrix size: 256 × 256; and slice thickness: 4.0 [mm]; imaging time approximately 1.5 min. T2-weighted images were not only used for anatomical reference but for the visual Pfirrmann grading of IVDs (24), which was performed by two radiologists (M.K. and A.K., 5 and 17 years of experience, respectively) in consensus.

QSI was performed by using a spin-echo diffusion-weighted echo-planar imaging sequence with the following parameters: TR: 5000 [ms]; TE: 99.6 [ms]; NEX: 3; FOV: 25.6 [cm]; matrix size: 128 × 128; slice thickness: 4.0 [mm]; imaging time approximately 7.5 min; and 11 b values (0, 40, 160, 360, 640, 1000, 1440, 1960, 2560, 3240, 4000 [s/mm^2]) with diffusion encoding in three directions (in the x, y, and z directions,) for every b value. The data from the three directions were acquired separately and then averaged. Corresponding q values for each b value were 59.5, 119.0, 178.6, 238.1, 297.6, 357.1, 416.7, 476.92, 535.7, and 595.2 cm^{-1}, respectively. Gradient length (δ) and the time between the two leading edges of the diffusion gradient (Δ) were 33.9 and 39.9 ms, respectively.

A multiecho spin echo sequence was performed in the axial plane for T2 mapping data acquisition with the following parameters: TR: 1200 [ms]; TE: 7.9,

Table 2.
Morning and Evening ADC Values*

	Morning	Evening	*P* value
ROI 1	0.80 ± 0.18	0.84 ± 0.25	0.58
ROI 2	1.46 ± 0.27	1.45 ± 0.25	0.75
ROI 3	1.69 ± 0.29	1.56 ± 0.32	< 0.01*
ROI 4	1.44 ± 0.28	1.45 ± 0.30	0.61
ROI 5	0.90 ± 0.25	0.85 ± 0.21	0.40

Shown are the results of the ADC value (10^{-3} mm^2/s) paired t-test analysis separated for region-of-interest localization. Data are presented as the mean ± standard deviation. There was a significant decrease in the ADC value in the middle of the nucleus pulposus (ROI 3) in the evening (< 0.05). No significant differences between the morning and the evening were observed in other areas.

Table 3.
Morning and Evening RMSD Values

	Morning	Evening	*P* value
ROI 1	24.4 ± 1.0	24.5 ± 1.1	0.70
ROI 2	37.8 ± 5.2	36.9 ± 5.3	0.51
ROI 3	45.2 ± 2.9	40.0 ± 3.0	< 0.01*
ROI 4	39.5 ± 5.0	39.9 ± 4.6	0.49
ROI 5	26.6 ± 3.0	25.7 ± 1.7	0.35

The results of the RMSD value (μm) paired t-test analysis separated for region-of-interest localization are presented. Data are displayed as the mean ± standard deviation. There was a significant decrease in the RMSD value in the middle of the nucleus pulposus (ROI 3) in the evening (< 0.05). No significant differences between the morning and the evening were observed in other areas.

Table 4.
Morning and Evening AKC Values

	Morning	Evening	*P* value
ROI 1	3.42 ± 0.73	3.27 ± 0.86	0.38
ROI 2	0.71 ± 0.14	0.76 ± 0.20	0.34
ROI 3	0.58 ± 0.04	0.67 ± 0.08	< 0.01*
ROI 4	0.74 ± 0.27	0.69 ± 0.13	0.23
ROI 5	2.86 ± 0.82	2.76 ± 0.82	0.42

The results of the AKC value paired t-test analysis separated for region-of-interest localization are shown. Data are presented as the mean ± standard deviation. There was a significant increase in the AKC value in the middle of the nucleus pulposus (ROI3) in the evening (< 0.05). No significant differences between the morning and the evening were observed in other areas.

15.8, 23.8, 31.7, 39.6, 47.5, 55.4, 63.4 [ms]; NEX: 0.5; FOV: 22 [cm]; matrix size: 256 × 256; slice thickness: 5.0 [mm]; imaging time approximately 2.5 min. This is one of the most common types of sequence for human in vivo spine T2 mapping and was used in a similar manner by other investigators as well (25).

Region of Interest Settings

We decided to measure five equally sized circular regions of interest (ROIs) on the central slice of the axial plane to allow us to evaluate the ROIs in a standardized and reproducible way in accordance with previously published literature (Fig. 1) (9). Each ROI measured 20% of the midline disc diameter (4–6 mm). The ROIs were manually drawn by a radiologist (M.K., 5 years of experience) using T2-weighted axial and sagittal images as an anatomical reference. Structures outside of the IVD, such as cerebrospinal fluid and retroperitoneal tissue, were carefully avoided. It is challenging to clearly define what tissue each ROI represents within the IVD because the transition from AF to NP tissue is usually gradual; however, the most anterior and most posterior ROIs (ROI 1 and ROI 5) were interpreted to represent anterior and posterior AF tissue, respectively. The ROIs in between were interpreted to represent nucleus tissue (ROI 2, anterior NP; ROI 3, middle NP; ROI 4, posterior NP).

Imaging Analysis

T2 maps were created with Functool software (Advantage Windows Workstation, General Electric), and T2 values were measured using the free software Image J (available at: rsbweb.nih.gov/ij/).

Q-space analyses were performed using the free software dTV II FZR and Volume-One 1.72 (Image Computing and Analysis Laboratory, Department of Radiology, The University of Tokyo Hospital, Tokyo, Japan; available at: http://www.ut-radiology.umin.jp/people/masutani/dTV.htm and http://www.volume-one.org/, respectively).

ADC maps (Fig. 2a) based on the conventional mono-exponential model were calculated first. ADC could be calculated by using part of the q-space data because the QSI data included multiple sets of b value data.

Next, the full widths at half maximum (FWHM) of PDF (Fig. 2b) and mean AKC maps (Fig. 2c) were obtained. Detailed new diffusion metrics and their calculation procedures were as previously described (15–22,26). Briefly, the key principle in q-space analysis is that a Fourier transformation of the signal attenuation with respect to q (or the b value) provides the PDF for diffusion by using multiple q values (16). The shape of the computed PDF can be characterized by the FWHM and the maximum height of the curve. In the specific case of an unrestricted Gaussian diffusion, the diffusion constant *D* and the RMSD for one

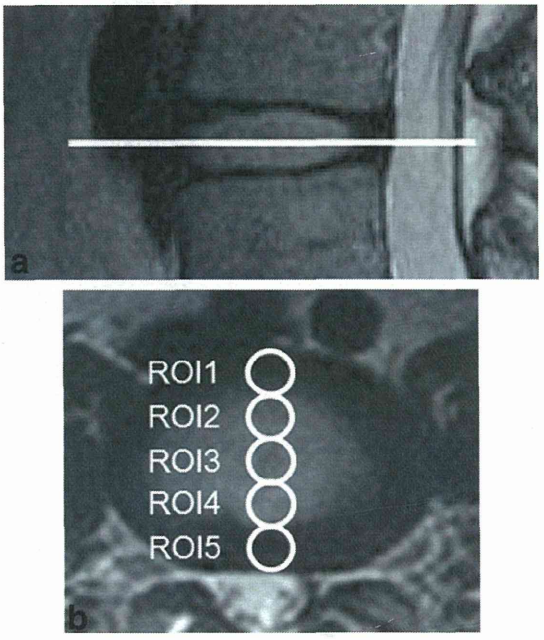

Figure 1. Positioning of the regions of interest (ROIs). The T2-weighted sagittal (a) and axial (b) images were used as anatomical references. Five equally sized circular ROIs (b) were manually drawn on the central slice of the axial planes (a, solid line) by a radiologist (M.K.), and were copied on the T2 maps and q-space images. Each ROI measured 20% of the midline disc diameter in the axial plane. The most anterior and most posterior ROIs (ROI 1 and ROI 5) were interpreted as anterior and posterior AF tissue, respectively. The ROIs in between were interpreted as nucleus tissue (ROI 2, anterior NP; ROI 3, middle NP; ROI 4, posterior NP).

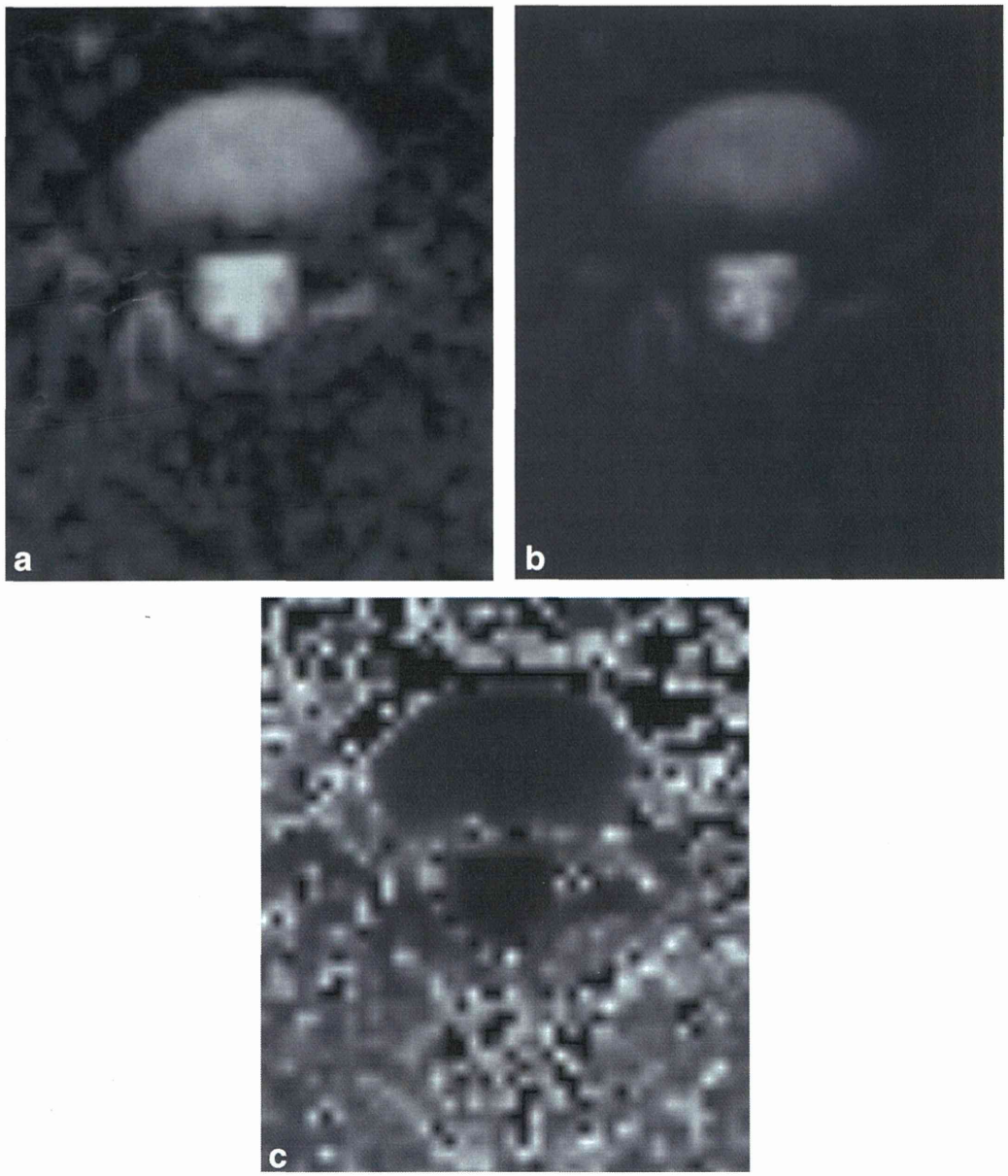

Figure 2. Diffusion metric maps: ADC (a); full width at half maximum of probability density function (b); AKC (c) of the IVD in the axial plane, acquired in the morning from one of the subjects (23-year-old male; body mass index, 21.8).

dimensional diffusion can be computed from the FWHM. Mean RMSD was calculated from the FWHM values (RMSD = 0.425 × FWHM) (17,18). Moreover, the AKC for a single direction can be determined by acquiring data at three or more b values (including b = 0) and fitting them to Eq. [1] as described previously (19):

$$\ln[S(b)]=\ln[S(0)]-bD_{app}+1/6b^2\times D_{app}\times K_{app} \quad [1]$$

where D_{app} is the apparent diffusion coefficient for the given direction and K_{app} is the apparent kurtosis coefficient, which is dimensionless.

Statistical Analysis

The data were analyzed using JMP 9.0.0 software (SAS Institute, Cary, NC). Paired t-tests were applied for assessing significant changes in T2 values and diffusion values (ADC, RMSD, and AKC) between the morning and the evening. A P value < 0.05 was considered to be significant.

RESULTS

The consensus panel classified the L4/5 discs of all subjects as Pfirrmann grade I, meaning there were no degenerative changes (24). T2, ADC, RMSD, and AKC values within each ROI were recorded (data are presented as mean ± standard deviation [SD]) in the morning and in the evening. These values are shown in Tables 1–4 and Figure 3. T2, ADC, and RMSD values showed a significant decrease in the evening (175.8 ± 49.5 ms, 1.56 ± 0.32 $10^{-3}mm^2/s$ and 40.0 ± 3.0 μm,

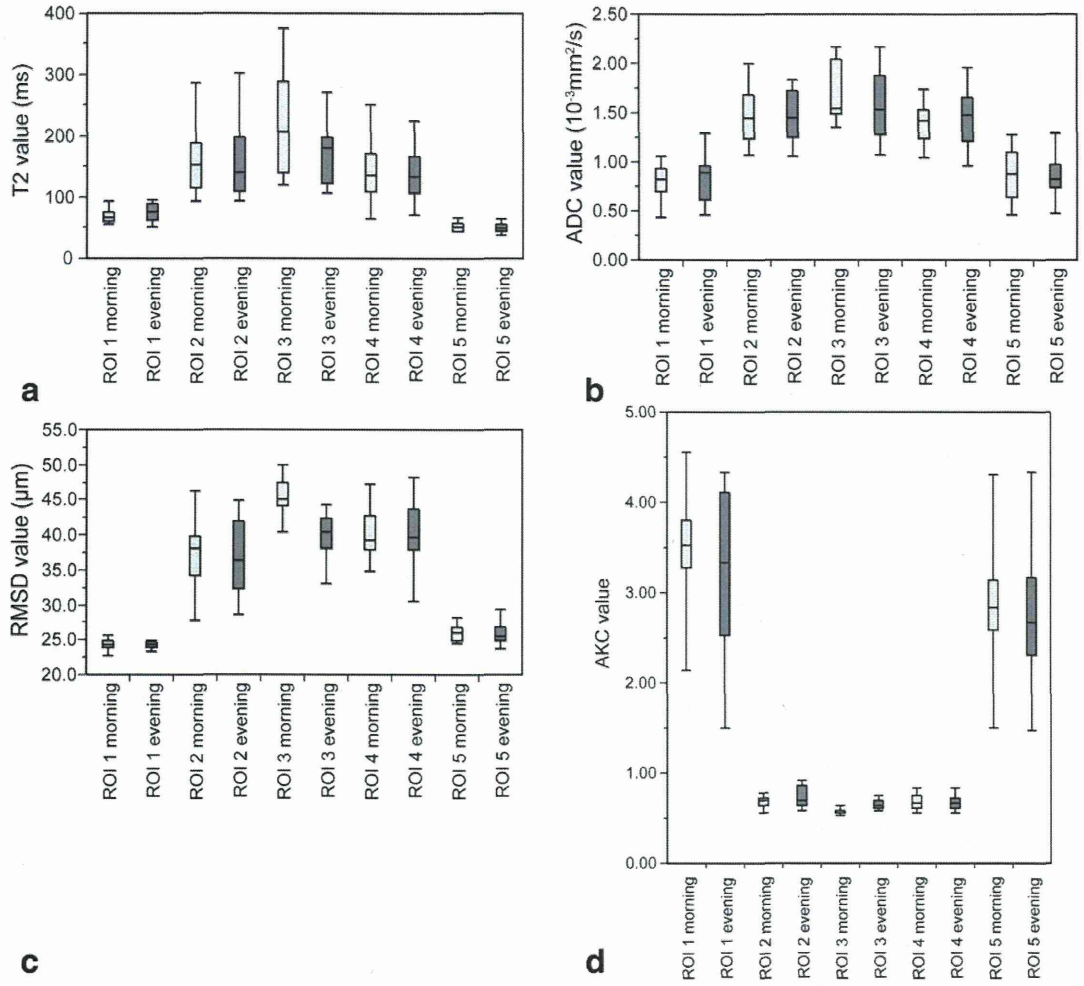

Figure 3. Box plots of T2 (a), ADC (b), RMSD (c), and AKC (d) values within each ROI in the morning and in the evening. Boxes represent the 25th and 75th percentile.

respectively; $P < 0.05$) for all values when compared with the morning values (226.5 ± 83.8 ms, 1.69 ± 0.29 $10^{-3}mm^2/s$ and 45.2 ± 2.9 μm, respectively; $P < 0.05$) in ROI 3 (representing the middle of the nucleus pulposus). In contrast, the AKC value in ROI 3 showed a significant increase in the evening (0.67 ± 0.08), when compared with the morning value (0.58 ± 0.04). No significant differences were observed between the morning and evening in the remaining ROIs.

DISCUSSION

In the present study, changes in T2 values and diffusion metrics of QSI data in IVDs before and after a diurnal load cycle were investigated. T2, ADC, and RMSD metrics in the evening were significantly lower than those in the morning, while the AKC value showed a significant increase in the evening, compared with the morning in the middle of the NP. No significant differences were observed between the morning and the evening in other areas.

Our finding of decreased T2 values after a diurnal load in the middle of the NP is consistent with those of previous reports (8,9). Only Ludescher et al reported on the diurnal ADC value changes of IVD using a 1.5T scanner, which revealed an decrease in the AF and no significant change in the NP (9). However, ADC values from all lumbar IVDs were averaged and analyzed together in their study, and they did not conduct subanalysis at each disc level or in each ROI position (e.g., anterior AF versus posterior AF). Because the compressive force distribution during daily activity should vary according to the disc level and position within each IVD, diurnal changes of diffusion metrics should be analyzed individually.

Our results showed decreased ADC and RMSD values and increased AKC values in the middle of the NP after a diurnal load. Water molecule diffusion is restricted in a complex manner by several factors such as the extracellular matrix (e.g., collagen fibers and proteoglycan) in the IVDs. In general, RMSD is not influenced by the viscosity of water, but by the space for free water movement (13,14). AKC describes the deviation of the water diffusion pattern within a voxel from a Gaussian distribution, which is thought to reflect the changes in microstructural complexity. Our results suggest that compressive forces occurring

during the day cause narrowing of the space for free water movement and a generally higher degree of microstructural complexity, which we are unable to assess with conventional quantitative MR measurements such as T2 or ADC. Diffusion metrics obtained from QSI data may provide additional information with regards to the diurnal microstructural changes occurring in the IVDs, such as matrix composition and integrity.

Several other factors are known to influence IVD quantitative MR measurements, namely, age-related changes and degenerative changes. Previous studies revealed decreasing T2 and ADC values of the NP with increasing age or with progression in the Pfirrmann grade (10,11,24). Karakida et al also found that no significant diurnal T2 value changes could be observed in degenerated discs (8), and they speculated that proteoglycan reduction in the NP with age and disc degeneration reduces not only the capability of holding fluid in the disc, but also the ability to recover the amount of fluid from daily compression force. In the present study, we controlled the age of subjects (mean age of the subjects was 27.3 years), and the degenerative grade of the IVDs (all IVDs included in the study were classified as Pfirrmann grade I, meaning no degenerative changes). Therefore, diurnal changes were investigated with minimal confounding factors. The young and homogenous background of our study group did provide an advantage to minimize potential confounding factors; however, future QSI studies should include assessment of age-related and degenerative changes and various IVD pathologies. QSI may also be applied to assessment of articular cartilage changes. Studies evaluating disc and cartilage changes with different amounts of workload and mechanical stress (e.g., exercise in athletes) with QSI are also awaited. In particular, the potential of QSI as a biomarker for detecting early structural disturbances, when these changes are not visible with conventional MR imaging and before clinical symptoms become evident, should be investigated as well.

One potential limitation of this study is the relatively low maximum b value ($b = 4000$ s/mm^2) that we used to calculate RMSD using q-space analysis. However, using higher b values (or q values) leads to fatal image degradation. We, therefore, decided to evaluate the changes in the RMSD values, rather than the absolute values themselves. Another limitation is partial volume which could have effected on the measurements especially at peripheral part of lumbar disc. However, during ROI selections, structures outside of the IVD, such as cerebrospinal fluid and retroperitoneal tissue, were carefully avoided.

In conclusion, the RMSD and AKC values obtained from QSI analysis may be sensitive biomarkers for IVD diurnal microstructural changes, namely the space for free water movement and microstructural complexity, in which we are unable to assess with conventional diffusion-weighted imaging metrics based on an assumption of a Gaussian shape and model of water molecules. Potentially, this technique can become an appropriate tool to allow characterization of IVD microstructural integrity.

ACKNOWLEDGMENT

Authors state that there is no financial relationship to disclose.

REFERENCES

1. Mwale F, Iatridis JC, Antoniou J. Quantitative MRI as a diagnostic tool of intervertebral disc matrix composition and integrity. Eur Spine J 2008;17(Suppl 4):432–440.
2. Marchand F, Ahmed AM. Investigation of the laminate structure of lumbar disc annulus fibrosus. Spine (Phila Pa 1976) 1990;15:402–410.
3. De Puky P. The physiological oscillation of the length of the body. Acta Orthop Scand 1935;6:338–348.
4. Krag MH, Cohen MC, Haugh LD, Pope MH. Body height change during upright and recumbent posture. Spine (Phila Pa 1976) 1990;15:202–207.
5. Eklund JA, Corlett EN. Shrinkage as a measure of the effect of load on the spine. Spine (Phila Pa 1976) 1984;9:189–194.
6. Reilly T, Tyrell A, Troup JDG. Circadian variation in human stature. Chronobiol Int 1984;1:121–126.
7. Roberts N, Hogg D, Whitehouse GH, Dangerfield P. Quantitative analysis of diurnal variation in volume and water content of lumbar intervertebral discs. Clin Anat 1998;11:1–8.
8. Karakida O, Ueda H, Ueda M, Miyasaka T. Diurnal T2 value changes in the lumbar intervertebral discs. Clin Radiol 2003;58:389–392.
9. Ludescher B, Effelsberg J, Martirosian P, et al. T2- and diffusion-maps reveal diurnal changes of intervertebral disc composition: an in vivo MRI study at 1.5 Tesla. J Magn Reson Imaging 2008;28:252–257.
10. Niu G, Yang J, Wang R, Dang S, Wu EX, Guo Y. MR imaging assessment of lumbar intervertebral disk degeneration and age-related changes: apparent diffusion coefficient versus T2 quantitation. AJNR Am J Neuroradiol 2011;32:1617–1623.
11. Zhang Z, Chan Q, Anthony MP, et al. Age-related diffusion patterns in human lumbar intervertebral discs: a pilot study in asymptomatic subjects. Magn Reson Imaging 2012;30:181–188.
12. Kärger J. NMR self-diffusion studies in heterogeneous systems. Adv Colloid Interface Sci 1985;23:129–148.
13. Cory DG, Garroway AN. Measurement of translational displacement probabilities by NMR: an indicator of compartmentation. Magn Reson Med 1990;14:435–444.
14. Callaghan PT, Coy A, MacGowan D, Packer KJ, Zelaya FO. Diffraction-like effects in NMR diffusion studies of fluids in porous solids. Nature 1991;351:467–469.
15. Assaf Y, Ben-Bashat D, Chapman J, et al. High b-value q-space analyzed diffusion-weighted MRI: application to multiple sclerosis. Magn Reson Med 2002;47:115–126.
16. Farrell JA, Smith SA, Gordon-Lipkin EM, Reich DS, Calabresi PA, van Zijl PCM. High b-value q-space diffusion-weighted MRI of the human cervical spinal cord in vivo: feasibility and application to multiple sclerosis. Magn Reson Med 2008;59:1079–1089.
17. Hori M, Motosugi U, Fatima Z, et al. A comparison of mean displacement values using high b-value Q-space diffusion-weighted MRI with conventional apparent diffusion coefficients in patients with stroke. Acad Radiol 2011;18:837–841.
18. Hori M, Fukunaga I, Masutani Y, et al. New diffusion metrics for spondylotic myelopathy at an early clinical stage. Eur Radiol 2012;22:1797–1802.
19. Jensen JH, Helpern JA, Ramani A, Lu H, Kaczynski K. Diffusional kurtosis imaging: the quantification of non-gaussian water diffusion by means of magnetic resonance imaging. Magn Reson Med 2005;53:1432–1440.
20. Wu EX, Cheung MM. MR diffusion kurtosis imaging for neural tissue characterization. NMR Biomed 2010;23:836–848.
21. Raab P, Hattingen E, Franz K, Zanella FE, Lanfermann H. Cerebral gliomas: diffusional kurtosis imaging analysis of microstructural differences. Radiology 2010;254:876–881.
22. Jensen JH, Falangola MF, Hu C, et al. Preliminary observations of increased diffusional kurtosis in human brain following recent cerebral infarction. NMR Biomed 2011;24:452–457.
23. Clark CA, Le Bihan D. Water diffusion compartmentation and anisotropy at high b values in the human brain. Magn Reson Med 2000;44:852–859.

24. Pfirrmann CW, Metzdorf A, Zanetti M, Hodler J, Boos N. Magnetic resonance classification of lumbar intervertebral disc degeneration. Spine (Phila Pa 1976) 2001;26:1873–1878.
25. Stelzeneder D, Welsch GH, Kovacs BK, et al. Quantitative T2 evaluation at 3.0T compared to morphological grading of the lumbar intervertebral disc: a standardized evaluation approach in patients with low back pain. Eur J Radiol 2012; 81:324–330.
26. Hori M, Fukunaga I, Masutani Y, et al. Visualizing non-Gaussian diffusion: clinical application of q-space imaging and diffusional kurtosis imaging of the brain and spine. Magn Reson Med Sci 2012;11:221–233.

ORIGINAL RESEARCH

Reduction of false positives at vessel bifurcations in computerized detection of lung nodules

Yukihiro Nomura[1], Mitsutaka Nemoto[1], Yoshitaka Masutani[2], Shouhei Hanaoka[3], Takeharu Yoshikawa[1], Soichiro Miki[1], Eriko Maeda[1], Naoto Hayashi[1], Naoki Yoshioka[4], Kuni Ohtomo[3]

1. Department of Computational Diagnostic Radiology and Preventive Medicine, the University of Tokyo Hospital, Tokyo, Japan. 2. Graduate School of Information Sciences, Hiroshima City University, Hiroshima, Japan. 3. Department of Radiology, the University of Tokyo Hospital, Tokyo, Japan. 4. Department of Radiology, Sanno Hospital, Tokyo, Japan.

Correspondence: Yukihiro Nomura. Address: Department of Computational Diagnostic Radiology and Preventive Medicine, The University of Tokyo Hospital, 7-3-1 Hongo, Bunkyo-ku, Tokyo 113-8655, Japan. E-mail: nomuray-tky@umin.ac.jp

Received: April 3, 2014 **Accepted:** July 4, 2014 **Online Published:** July 15, 2014
DOI: 10.5430/jbgc.v4n3p36 **URL:** http://dx.doi.org/10.5430/jbgc.v4n3p36

Abstract

Objective: We describe a new false positive (FP) reduction method based on surface features in our computerized detection system for lung nodules and evaluate the method using clinical chest computed tomography (CT) scans.

Methods: In our detection method, nodule candidates are extracted using volumetric curvature-based thresholding and region growing. For various sizes of nodules, we adopt multiscale integration based on Hessian eigenvalues. For each nodule candidate, two surface features are calculated to differentiate nodules and FPs at vessel bifurcations. These features are fed into a quadratic classifier based on the Mahalanobis distance ratio.

Results: In an experimental study involving 16 chest CT scans, the average number of FPs was reduced from 107.5 to 14.1 per case at 90% sensitivity.

Conclusions: This proposed FP reduction method is effective in removing FPs at vessel bifurcations.

Key words

Surface feature, Vessel bifurcation, Lung nodule, Chest CT, Computer-assisted detection

1 Introduction

Lung cancer is one of the most difficult cancers to cure, and early detection is necessary to improve patient outcomes [1, 2]. Chest computed tomography (CT) can help detect lung cancer at an earlier stage than chest radiography [3]. The recent development of multidetector-row CT (MDCT) has allowed the acquisition of thin-section images of a whole lung during a single breath hold [4]. However, due to the large number of images generated by chest MDCT examination, reading by radiologists is time-consuming and may result in missed nodules. Therefore, computer-assisted detection (CAD) systems for lung nodules in chest CT images have been developed to assist radiologists.

A number of research groups have reported a variety of CAD systems for detecting lung nodules in chest CT images, including multiple grayscale thresholding [5, 6], local density maximum algorithm [7], fuzzy clustering [8], genetic algorithm

template matching of Gaussian spheres and discs [9], filters enhancing spherical structures [10-13], curved surface morphology analysis [14], and volumetric curvature-based thresholding and region growing [15]. Commercial CAD systems for detecting lung nodules in chest CT images have also been developed, including the ImageChecker CT Lung system (R2 Technology Inc., Sunnyvale, CA, USA), Lung VCAR (GE Healthcare Technologies, Waukesha, WI, USA), and Syngo Lung CAD (Siemens Medical Solutions, Erlangen, Germany).

Although these CAD systems detect lung nodules with high sensitivity, results may include false positives (FPs). These typically occur at vessel bifurcations, sharply curved vessels, artifacts due to respiratory or cardiac motion, abnormalities on the pleura (scars and fluid build-up), and so forth [16-19]. Among these, vessel bifurcations are of particular importance, and reducing FPs occurring at vessel bifurcations would considerably improve the detection performance. In our CAD system for lung nodules [20], for example, almost half the FPs occur at vessel bifurcations.

In this paper, we propose a new FP reduction method based on surface features in our CAD system for lung nodules. We then evaluate the method using 16 clinical cases.

2 Methods

2.1 Overview of detection method

Figure 1 shows a flowchart of our detection method, which consists of three steps: preprocessing, nodule candidate extraction, and FP reduction. The preprocessing step involves isotropic resampling, lung segmentation, binarization of the lung volume, and surface extraction from the binarized lung volume. The nodule candidate extraction step involves thresholding based on the shape index value and shape-index-based region growing [20]. For various sizes of nodules, we adopted multiscale integration based on Hessian eigenvalues. Finally, the FP reduction step defines two surface features and calculates them for each nodule candidate. These feature values are fed into a quadratic classifier based on the Mahalanobis distance ratio.

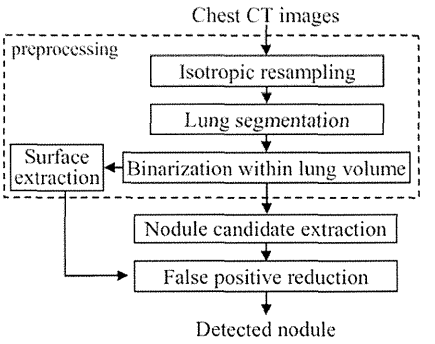

Figure 1. Flowchart of the detection method

2.2 Preprocessing

Chest CT images are resampled using trilinear interpolation to obtain the isotropic volume. The resampled voxel size is equal to the pixel size of the CT slice. After that, lung segmentation is carried out. The processing procedures of lung segmentation are described as follows:

1) The initial lung mask $\mathbf{L}_{init}$ is extracted as a set of connected voxels with CT values lower than -600 HU.
2) A gray-scale histogram of the voxels in $\mathbf{L}_{init}$ is generated, and the peak CT value in the histogram T_{peak} is obtained.
3) The initial mask for the trachea and large airways is extracted as the set of connected voxels with CT values lower than T_{peak} +50 HU and smoothed by opening with a spherical kernel of 2.5-voxel radius.

4) The final mask for the trachea and large airways is obtained as a superiormost connected component and dilated by a spherical kernel of 2.5-voxel radius.

5) After the removal of the mask for the trachea and large airways from the initial lung mask, closing with a spherical kernel of 5-voxel radius is applied to the masks for the left and right lungs to include lung nodules and pulmonary vessels.

6) Removal of the mask for the bones from the masks for the left and right lungs is carried out. The mask for the bones is extracted as the largest connected component with CT values higher than 100 HU, and then closing with a spherical kernel of 2.5-voxel radius and dilation with a spherical kernel of 1.5-voxel radius are carried out.

7) The lung volume **L** is obtained as the intersection voxels between the chest CT volume and the masks for the left and right lungs.

After lung segmentation, binarization within **L** is carried out again to extract the region of nodules and vessels. The binarized lung volume $\mathbf{L}_{bin}$ is given by:

$$\mathbf{L}_{bin} = \{p \mid I(\mathbf{x}) \geq T_{CT}, p \in \mathbf{L}\} \tag{1}$$

where $I(\mathbf{x})$ is the CT value (HU) of voxel p and $\mathbf{x}$ is the 3D coordinate for the position of voxel p. T_{CT} is the threshold for the extraction of vessels and nodules. Moreover, the surface areas of vessels and nodules $\mathbf{L}_{sf}$ are extracted using:

$$\mathbf{L}_{sf} = \mathbf{L}_{bin} - (\mathbf{L}_{bin} \circ \mathbf{K}_{1.0}) \tag{2}$$

where $\circ$ defines erosion and $\mathbf{K}_{1.0}$ is a spherical kernel of 1-voxel radius.

2.3 Extraction of nodule candidates

The shape index is calculated at the voxels of $\mathbf{L}_{bin}$ using original CT values. The shape index $S(\mathbf{x}, \sigma)$ is defined as follows [21, 22]:

$$S(\mathbf{x},\sigma) = \frac{1}{2} - \frac{1}{\pi}\arctan\frac{k_1(\mathbf{x},\sigma)+k_2(\mathbf{x},\sigma)}{k_1(\mathbf{x},\sigma)-k_2(\mathbf{x},\sigma)} \tag{3}$$

$$\begin{aligned} k_1(\mathbf{x},\sigma) &= H(\mathbf{x},\sigma)+\sqrt{H^2(\mathbf{x},\sigma)-K(\mathbf{x},\sigma)} \\ k_2(\mathbf{x},\sigma) &= H(\mathbf{x},\sigma)-\sqrt{H^2(\mathbf{x},\sigma)-K(\mathbf{x},\sigma)} \end{aligned} \tag{4}$$

where k_1 and k_2 are principal curvatures ($k_1 \geq k_2$), H is the mean curvature, K is the Gaussian curvature, and σ (voxel) is the standard deviation of the Gaussian filter. S ranges from 0 to 1. Figure 2 shows the relation between the S value and shape type. The S values of the voxels of a typical nodule range from 0.8 to 1.0, showing a peak or dome, whereas those of a vessel range from 0.5 to 0.75, showing a ridge or saddle. Therefore, thresholding based on the S value differentiates nodules and vessels.

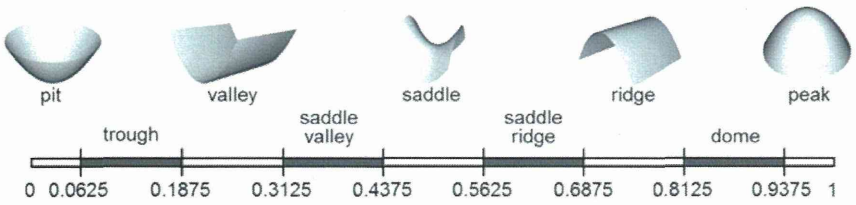

Figure 2. Relation between shape index value and shape type

ISSN 1925-4008 E-ISSN 1925-4016

Figure 3 shows the relationship between σ/R_{eff} and the mean S value in two isolated nodules, where R_{eff} is the volume-equivalent spherical radius for the nodule. If σ is smaller than R_{eff}, the mean S value of nodules corresponding to the shape type of the nodule represents the "peak" value. In contrast, if σ is larger than R_{eff}, the mean S value is markedly degraded due to the smoothing effect of the Gaussian filter. We observed a similar tendency in 12 other isolated nodules. Multiscale integration [23] is desirable to obtain an appropriate shape index value because various sizes of nodules exist in chest CT images.

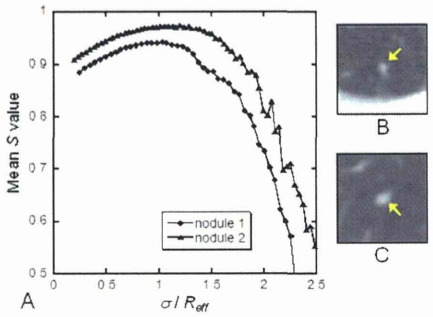

Figure 3. (A) Relationship between σ/R_{eff} and mean S value (R_{eff}: volume-equivalent spherical radius for nodule). (B) Axial section of nodule 1 (R_{eff} = 2.0 voxels). (C) Axial section of nodule 2 (R_{eff} = 2.7 voxels).

In this paper, we adopted multiscale integration based on Hessian eigenvalues [24, 25] to obtain $S_{opt}(\mathbf{x})$. The Hessian at voxel p is given as follows:

$$\mathbf{H}(\mathbf{x},\sigma)=\begin{bmatrix} I_{xx}(\mathbf{x},\sigma) & I_{xy}(\mathbf{x},\sigma) & I_{xz}(\mathbf{x},\sigma) \\ I_{yx}(\mathbf{x},\sigma) & I_{yy}(\mathbf{x},\sigma) & I_{yz}(\mathbf{x},\sigma) \\ I_{zx}(\mathbf{x},\sigma) & I_{zy}(\mathbf{x},\sigma) & I_{zz}(\mathbf{x},\sigma) \end{bmatrix} \tag{5}$$

where the partial second derivatives of $I(\mathbf{x})$ are represented by expressions such as:

$$I_{xx}(\mathbf{x},\sigma)=\left\{\frac{\partial^2}{\partial x^2}G(\sigma)\right\}*I(\mathbf{x}) \tag{6}$$

$$I_{xy}(\mathbf{x},\sigma)=\left\{\frac{\partial^2}{\partial x\partial y}G(\sigma)\right\}*I(\mathbf{x}) \tag{7}$$

$G(\sigma)$ is a 3D Gaussian function with standard deviation σ. Let the eigenvalues of $\mathbf{H}$ be λ_1, λ_2, and λ_3 ($|\lambda_1| \geq |\lambda_2| \geq |\lambda_3|$). On the basis of these eigenvalues, a local pattern is classified as a plate-like, line-like, or blob-like structure. Table 1 summarizes the relation between λ_1, λ_2, and λ_3 for different structures. Given that the CT values of nodules and vessels are higher than those of the pulmonary parenchyma, the sign of λ_1 at a voxel within a nodule or vessel is generally negative. In our multiscale integration, Hessian eigenvalues are calculated for several values of σ, and $\sigma_{opt}(\mathbf{x})$ is determined as follows:

$$\sigma_{opt}(\mathbf{x})=\arg\min_{\sigma}\left(\sigma^{\gamma}\lambda_1(\mathbf{x},\sigma)\right) \tag{8}$$

where γ is a parameter for normalization [23-26]. Then, $S_{opt}(\mathbf{x})$ is calculated as follows:

$$S_{opt}(\mathbf{x})=S\left(\mathbf{x},\sigma_{opt}(\mathbf{x})\right) \tag{9}$$

After calculating S_{opt}, the sets of connected voxels with signals higher than a given threshold of shape index value S_{high} are extracted. S_{high} is set to higher than 0.8 to reduce the influence of artifacts. Small components under a volume threshold T_{size} are then removed. If T_{size} is set too high, FPs caused by the artifacts as well as true nodules with a small size or nonspherical shape are removed. Finally, shape-index-based region growing is carried out in $\mathbf{L}_{bin}$. The termination criterion for region growing is set to $S_{low} \leq S_{opt} \leq 1.0$. S_{low} is set to a value that differentiates nodules from vessels, and $S_{low} < S_{high}$.

Table 1. Local pattern in relation to Hessian eigenvalues

Structure		λ_1	λ_2	λ_3
No noticeable structure		•	•	•
Plate-like	bright	–	•	•
	dark	+	•	•
Line-like	bright	–	–	•
	dark	+	+	•
Blob-like	bright	–	–	–
	dark	+	+	+

•: small eigenvalue, +: significant positive value, –: significant negative value.

2.4 FP reduction

In this section, we describe our FP reduction scheme developed for FPs at vessel bifurcations and its theoretical basis with examples of synthetic data analysis.

In the literature, curvature and Hessian eigenvalues, both based on second derivatives of a volumetric image function, are often employed for lung nodule detection [8, 11, 12, 14, 15, 20]. These two features have a certain relationship, derived from the fact that the principal curvatures in Equation 4 are calculated from the rotation transformation and eigenvalue analysis of the Hessian [27]. It is known that FPs in the detection of nodule-like structures based on curvature and Hessian eigenvalues also have a similar tendency.

Figure 4A shows synthetic volume data used to simulate a vessel bifurcation with Gaussian noise. The intensity levels of the vessel (foreground) and background were set to -200 and -900 HU, respectively, and the standard deviation of the Gaussian noise was 50. Figure 4B shows the shape index image. As shown in Figure 4B, the S_{opt} value at the center of the vessel bifurcation is high. Figure 4C shows the region of the nodule candidate obtained by our method.

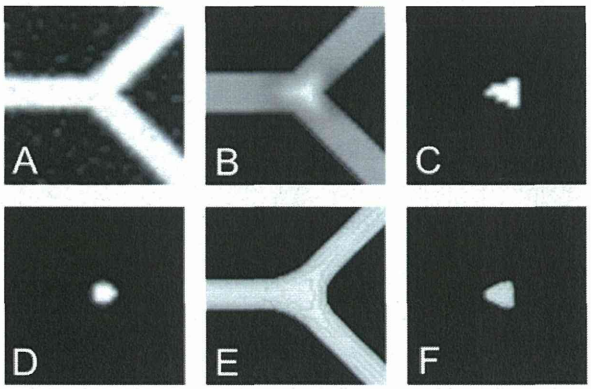

Figure 4. Examples of synthetic data analysis. (A) Synthetic volume data of vessel bifurcation with Gaussian noise, in which the vessel and background intensities are set to -200 and -900 HU, respectively, and the standard deviation of the Gaussian noise is 50. (B) Shape index image of A, in which a higher shape index is shown by a lighter gray-scale value. (C) Region of nodule candidate obtained by our method. (D) Enhanced image obtained by the dot-enhancement filter. (E) Isosurface of the Gaussian-smoothed image of the synthetic data (threshold: -700 HU). (F) Isosurface of the Gaussian-smoothed image of the synthetic data (threshold: -600 HU).

A similar result can be obtained using a Hessian-eigenvalue-based detection scheme. Figure 4D shows a dot-enhanced image applied to the image in Figure 4A based on Hessian eigenvalues [12]. The filter is defined as follows:

$$z_{blob}(\mathbf{x}) = \begin{cases} |\lambda_3|^2 / |\lambda_1| & \text{if } \lambda_1 < 0, \lambda_2 < 0, \lambda_3 < 0 \\ 0 & \text{otherwise} \end{cases} \tag{10}$$

As shown in Figure 4D, the center of the vessel bifurcation is enhanced by the filter, thereby yielding an FP due to its misclassification as a blob-like structure (see Table 1).

FPs at vessel bifurcations are inevitable in the detection of nodule-like structures using second-derivative-based features. This is a by-product of the Gaussian convolution employed for scale-matching. It is easily confirmed that Gaussian filtering forms or enhances a blob-like isosurface inside a vessel bifurcation (see Figures 4E and 4F). Without Gaussian filtering, however, it is impossible to obtain scale-matched features of target objects such as vessels and nodules. To remove these FPs, we utilize the spatial relationship between vessels and FPs based on the fact that the FP volume is limited to the center of a bifurcation, as shown in Figures 4B and 4D.

We first define the *surface exposure ratio* R_{SE} and *surface area to volume ratio* R_{SV} and calculate these features for each nodule candidate. Let $\mathbf{c}(i)$ denote the voxel set in the ith nodule candidate. $R_{SE}(i)$ and $R_{SV}(i)$ are defined by:

$$R_{SE}(i) = \frac{N_c(i)}{A(i)} \tag{11}$$

$$R_{SV}(i) = \frac{A(i)}{V(i)} \tag{12}$$

where $A(i)$ is the number of voxels of the surface area in $\mathbf{c}(i)$, that is, the number of voxels in $\mathbf{c}(i) - (\mathbf{c}(i) \circ \mathbf{K}_{1.0})$. $V(i)$ is the number of voxels included in $\mathbf{c}(i)$ and $N_c(i)$ is the number of intersection voxels of $\mathbf{L}_{sf}$ and $\mathbf{c}(i)$. In the case of FPs at a vessel bifurcation, $\mathbf{c}$ exists only at the center of the bifurcation (see Figures 5A-5C), while region $\mathbf{L}_{sf}$ exists only at the surface of the vessel (see Figure 5D). Therefore, R_{SE} is small since N_c is much smaller than A. $R_{SE} = 0.28$ and $R_{SV} = 0.79$ for the nodule candidate shown in Figure 5C. In contrast, in the case of a nodule, $\mathbf{c}$ includes almost the whole area of the nodule (see Figures 5E-5H). Therefore, R_{SE} is close to 1.0 since N_c is almost equal to A. $R_{SE} = 1.0$ and $R_{SV} = 0.61$ for the nodule candidate shown by Figure 5G. Figure 6A shows the R_{SV} - R_{SE} feature space for true positives (TPs) and FPs at the vessel bifurcation; as shown in this figure, it is expected that FPs at vessel bifurcations will be removed by using a classifier consisting of R_{SE} and R_{SV}.

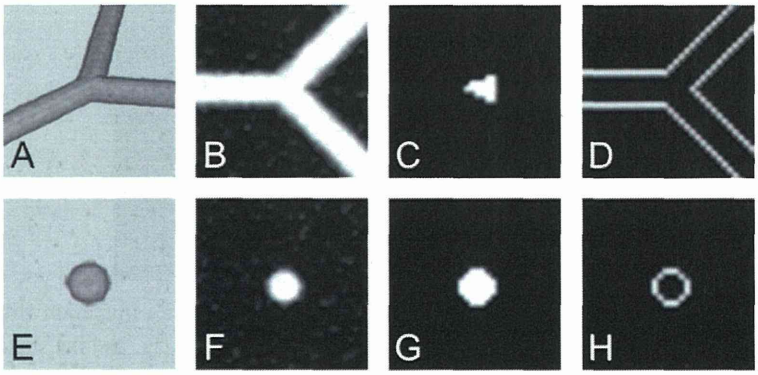

Figure 5. Examples of synthetic data analysis. (A) 3D volume rendering of a synthetic image of a vessel bifurcation using the same image parameters as in Figure 4A. (B) Image of an axial section of A. (C) Region of a nodule candidate obtained by our method. (D) Result of surface extraction. (E) 3D volume rendering of a synthetic image of a nodule with Gaussian noise, in which the nodule and background intensities are set to -200 and -900 HU, respectively, and the standard deviation of the Gaussian noise is 50. (F) Image of an axial section of E. (G) Region of nodule candidate obtained by our method. (H) Result of surface extraction.

The obtained values of R_{SE} and R_{SV} are fed into a quadratic classifier based on the Mahalanobis distance. From the Mahalanobis distance D_j (j = TP, FP), **c** is classified as belonging to either the TP or FP class. The Mahalanobis distance ratio R_M is defined as follows:

$$R_M = \frac{D_{FP}}{D_{TP}} \tag{13}$$

If R_M is below a certain threshold, **c** is classified as an FP and removed from the final results.

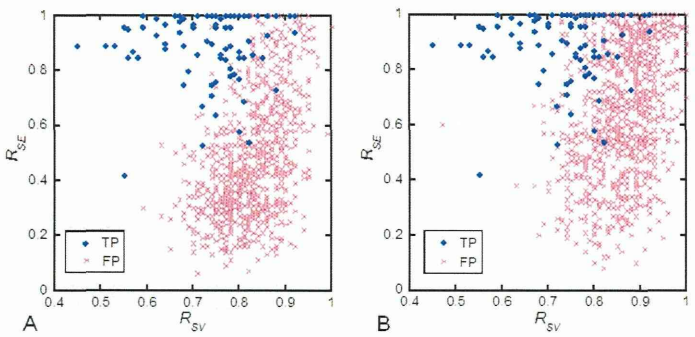

Figure 6. R_{SV} - R_{SE} feature space for T_{CT} = -700, T_{size} = 16, S_{high} = 0.9, and S_{low} = 0.8. (A) TPs and FPs at a vessel bifurcation. (B) TPs and FPs in other regions.

3 Results

This study was approved by the ethical review board of our institute. We evaluated the proposed FP reduction method using 16 chest CT scans acquired by MDCT scanners (Aquilion 16 or Aquilion 64, Toshiba, Tokyo, Japan). Each slice has a matrix size of 512 × 512 with a pixel size of 0.683 or 0.781 mm. The reconstruction interval is 1.0 mm. Two experienced radiologists identified 82 true nodules ranging from 3.0 mm to 12.5 mm in diameter. The nodules include four types of patterns: noncalcified solid, calcified solid, mixed ground-glass opacity (GGO), and pure GGO. Each CT scan included at least one true nodule. The performance of the detection method was evaluated using a leave-one-out cross-validation method.

In the extraction of nodule candidates, T_{CT} was experimentally set to -700 in order to detect all the identified true nodules. The range of σ in multiscale integration was experimentally set to {1, 2, 3, 4, 5} in consideration of the extraction performance, as discussed later. S_{low}, S_{high}, and γ were experimentally set to 0.8, 0.9, and 1.5, respectively.

Table 2 shows the FP reduction performance of our detection method at 80% and 90% sensitivities. As shown in Table 2, the number of FPs with T_{size} = 16 was 14.1 per case at 90% sensitivity and 4.8 per case at 80% sensitivity. The number of FPs in the step for nodule candidate extraction with T_{size} = 16 was 107.5 per case without false negatives (FNs). Figure 7 shows the free-response receiver operating characteristic (FROC) curves for different T_{size} values.

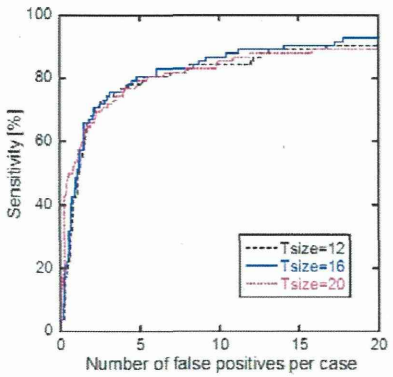

Figure 7. FROC curves for different T_{size} values

Table 2. FP reduction performance of our detection method

T_{size}	Sensitivity (%)	
	80	90
12	5.3	16.8
16	4.8	14.1
20	5.4	25.1

Figure 8 shows an example of a detection result using our detection method, revealing a marked reduction in FPs. Figure 9 shows an example of residual FPs in our detection method. Figure 9A shows the case of an aneurysm-like structure. Figure 9B shows the case of a mucus plug in a bronchus. Figure 10 shows an example of an FN in our detection method, which is the case of a juxtapleural nodule. A juxtapleural nodule is defined as a nodule having part of its circumference abutting a pleural surface, *i.e.*, a chest wall, diaphragm, mediastinum, or fissure [28].

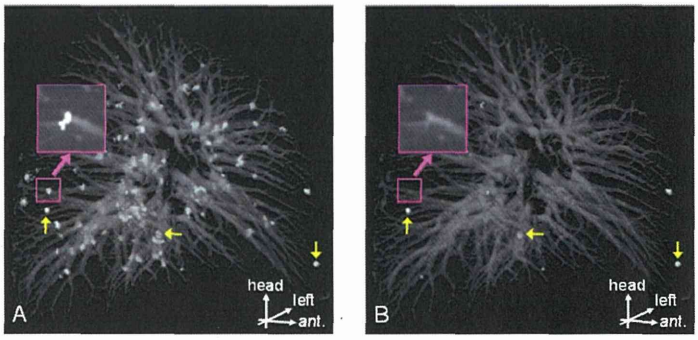

Figure 8. Example of detection result using our detection method. (A) Result of nodule candidate extraction with T_{size} = 16. (B) Result of FP reduction at 90% sensitivity. White regions with a yellow arrow indicate true nodules, and white regions without a yellow arrow show FPs.

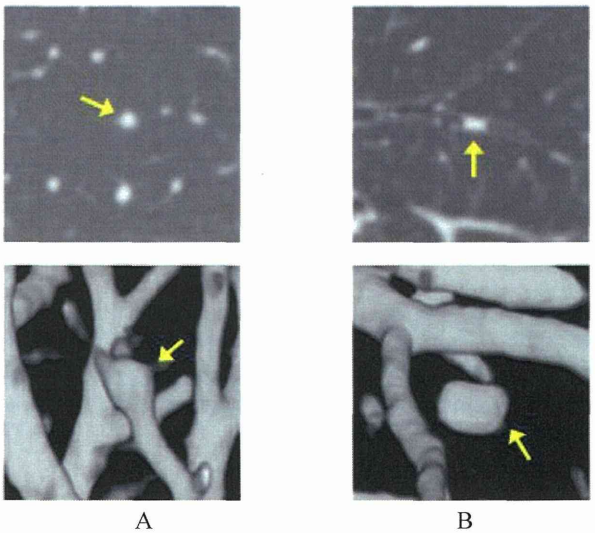

Figure 9. Example of residual FPs in our detection method. (A) Case of aneurysm-like structure. (B) Case of mucus plug in a bronchus. The top row shows the axial section and the bottom row shows the 3D volume rendering.

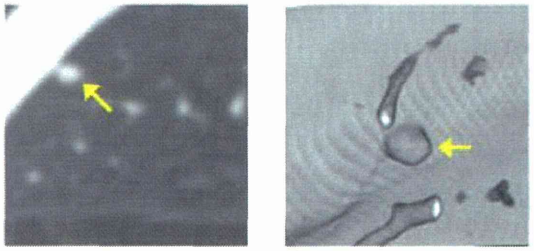

Figure 10. Example of FN in our detection method in the case of a juxtapleural nodule. The left image shows the axial section and the right image shows the 3D volume rendering.

4 Discussion

In this paper, we propose a surface-feature-based FP reduction method for eliminating FPs at vessel bifurcations. In our clinical study, the proposed method greatly contributed to reducing the number of FPs, from 107.5 to 14.1 per case at 90% sensitivity.

Many FPs with a low R_{SE} value occur in other regions, such as vessel crossings or bifurcations of the bronchial wall (see Figure 6B). Consequently, our proposed method is also effective in removing FPs in other regions with low R_{SE} values (see Figures 7 and 8). In addition, the proposed method is useful as an FP reduction method in Hessian-eigenvalue-based lung nodule detection (see Figure 4).

We experimentally set T_{CT} = -700 to detect all the identified nodules. The appropriate T_{CT} value depends on the data set. In particular, the existence of pure GGO nodules in data sets greatly affects the appropriate value of T_{CT} since GGO is defined as a hazily increased attenuation of the lung observed on CT images with preservation of the bronchiole and vascular margins [29, 30].

We experimentally set the range of σ in multiscale integration to {1, 2, 3, 4, 5}, although the maximum value of σ is smaller than the maximum radius of a nodule. If σ_{opt} is smaller than the radius of a nodule, the shape index of the nodule is an appropriate value corresponding to the shape type (see Figure 3). Similar methods for multiscale integration based on Hessian eigenvalues have been reported by Li *et al.* [12] and Sato *et al.* [25], in which the set of σ was selected such that σ_{k+1}/σ_k was approximately constant ($\sigma_k < \sigma_{k+1}$). We also investigated the set of σ of {1, 1.5, 2.25, 3.375, 5} and found that the shape index decreased markedly on the surface of nodules because of the overscaling of σ_{opt}. Moreover, the selected σ had a tendency to overscale with increasing γ [26]. To avoid the overscaling of σ_{opt}, we therefore set γ = 1.5.

If T_{size} is set too low, FPs with a small size are extracted as nodule candidates and fed into the classifier for FP reduction, and the number of FPs increases at 90% sensitivity (see Table 2 and Figure 7). On the other hand, if T_{size} is set too high, small or nonspherical true nodules are removed in nodule candidate extraction. Consequently, the value of T_{size} affects the overall performance of our detection method. Further improvement of our proposed method will require additional features for the effective removal of small FPs.

The removal of the residual FPs, as shown in Figure 9, is difficult owing to their nodule-like structure. The shapes of these FPs are similar to those of TPs and their R_{SE} values are close to 1.0. However, radiologists can differentiate between such FPs and true nodules by considering adjacent anatomical structures such as vessels and bronchi. Further improvement of our proposed FP reduction method will require additional features based on adjacent anatomical structures.

TPs with a low R_{SE} value result in FNs, as shown in Figure 6. The R_{SE} value is affected by the attachment of adjacent structures. The N_c values of nodules attached to adjacent structures are smaller than those of isolated nodules since the attachment is not extracted as part of the region $\mathbf{L}_{sf}$. Hence, the R_{SE} values of nodules attached to adjacent structures are smaller than those of isolated nodules. In particular, the degradation of the R_{SE} value typically occurs in the case of juxtapleural nodules, as shown in Figure 10. To further reduce FPs without eliminating TPs, we are currently developing an FP reduction method based on dual classifiers for juxtapleural and nonpleural nodules. The results of preliminary experiments indicate that dual classifiers have the potential to improve the performance of FP reduction.

We conclude that the surface-feature-based FP reduction method is effective in removing FPs at vessel bifurcations.

References

[1] Sone S, Takashima S, Li F, Yang Z, Honda T, Maruyama Y, *et al.* Mass screening for lung cancer with mobile spiral computed tomography scanner. Lancet. 1998 Apr; 351(9111): 1242-5. http://dx.doi.org/10.1016/S0140-6736(97)08229-9

[2] Nawa T, Nakagawa T, Kusano S, Kawasaki Y, Sugawara Y, Nakata H. Lung cancer screening using low-dose spiral CT: results of baseline and 1-year follow-up studies. Chest. 2002 Jul; 122(1): 15-20. PMid: 12114333. http://dx.doi.org/10.1378/chest.122.1.15

[3] Swensen SJ, Jett JR, Hartman TE, Midthun DE, Mandrekar SJ, Hillman SL, *et al.* CT screening for lung cancer: five-year prospective experience. Radiology. 2005 Apr; 235(1): 259-65. PMid: 15695622. http://dx.doi.org/10.1148/radiol.2351041662

[4] Kim JS, Kim JH, Cho G, Bae KT. Automated detection of pulmonary nodules on CT images: effect of section thickness and reconstruction interval -- initial results. Radiology. 2005 Jul; 236(1): 295-9. PMid: 15955863. http://dx.doi.org/10.1148/radiol.2361041288

[5] Giger ML, Bae KT, MacMahon H. Computerized detection of pulmonary nodules in computed tomography images. Invest Radiol. 1994 Apr; 29(4): 459-65. PMid: 8034453. http://dx.doi.org/10.1097/00004424-199404000-00013

[6] Armato SG, Giger ML, MacMahon H. Automated detection of lung nodules in CT scans: Preliminary results. Med Phys. 2001 Aug; 28(8): 1552-61. PMid: 11548926. http://dx.doi.org/10.1118/1.1387272

[7] Zhao B, Gamsu G, Ginsberg MS, Jiang L, Schwartz LH. Automatic detection of small lung nodules on CT utilizing a local density maximum algorithm. J Appl Clin Med Phys. 2003 Summer; 4(3): 248-60. PMid: 12841796. http://dx.doi.org/10.1120/1.1582411

[8] Kanazawa K, Kawata Y, Niki N, Satoh H, Ohmatsu H, Kakinuma R, *et al.* Computer-aided diagnosis for pulmonary nodules based on helical CT images. Comput Med Imaging Graph. 1998 Mar-Apr; 22(2): 157-67. http://dx.doi.org/10.1016/S0895-6111(98)00017-2

[9] Lee Y, Hara T, Fujita H, Itoh S, Ishigaki T. Automated detection of pulmonary nodules in helical CT images based on an improved template-matching technique. IEEE Trans Med Imaging. 2001 Jul; 20(7): 595-604. PMid: 11465466. http://dx.doi.org/10.1109/42.932744

[10] Miwa T, Kako J, Yamamoto S, Matsumoto M, Tateno Y, Iinuma T, *et al.* Automatic detection of lung cancers in chest CT images by the variable N-Quoit filter. Systems and Computers in Japan. 2002 Jan; 33(1): 53-63. http://dx.doi.org/10.1002/scj.1099

[11] Chang S, Emoto H, Metaxas DN, Axel L. Pulmonary micronodule detection from 3D chest CT. Lecture Notes in Computer Science. 2004 Sep; 3217: 821-8. http://dx.doi.org/10.1007/978-3-540-30136-3_100

[12] Li Q, Sone S, Doi K. Selective enhancement filters for nodules, vessels, and airway walls in two- and three-dimensional CT scans. Med Phys. 2003 Aug; 30(8): 2040-51. PMid: 12945970. http://dx.doi.org/10.1118/1.1581411

[13] Matsumoto S, Kundel HL, Gee JC, Gefter WB, Hatabu H. Pulmonary nodule detection in CT images with quantized convergence index filter. Med Image Anal. 2006 Jun; 10(3): 343-52. PMid: 16542867. http://dx.doi.org/10.1016/j.media.2005.07.001

[14] Taguchi H, Kawata Y, Niki N, Satoh H, Ohmatsu H, Kakinuma R, *et al.* Lung cancer detection based on helical CT images using curved surface morphology analysis. Proc. SPIE 3661, Medical Imaging. 1999: Image Processing, 1307 (May 21, 1999).

[15] Dehmeshki J, Ye X, Valdivieso M, Roddie M Costello J. Shape based region growing using derivatives of 3D medical images: application to automatic detection of pulmonary nodules. Proceedings of the 3rd International Symposium on Image and Signal Processing and Analysis (ISPA 2003). 18-20 Sep 2003; 2: 1118-23.

[16] Wiemker R, Rogalla P, Blaffert T, Sifri D, Hay O, Srinivas Y, *et al.* Computer-aided detection (CAD) and volumetry of pulmonary nodules on high-resolution CT data. Medicamundi. 2003 Nov; 47(3): 37-44.

[17] McCulloch CC, Kaucic RA, Mendonça PR, Walter DJ, Avila RS. Model-based detection of lung nodules in computed tomography exams. Thoracic computer-aided diagnosis. Acad Radiol. 2004 Mar; 11(3): 258-66. http://dx.doi.org/10.1016/S1076-6332(03)00729-3

[18] Das M, Mühlenbruch G, Mahnken AH, Flohr TG, Gündel L, Stanzel S, *et al.* Small pulmonary nodules: effect of two computer-aided detection systems on radiologist performance. Radiology. 2006 Nov; 241(2): 564-71. PMid: 17057074. http://dx.doi.org/10.1148/radiol.2412051139

[19] Saba L, Caddeo G, Mallarini G. Computer-aided detection of pulmonary nodules in computed tomography: analysis and review of the literature. J Comput Assist Tomogr. 2007 Jul-Aug; 31(4): 611-9. PMid: 17882043. http://dx.doi.org/10.1097/rct.0b013e31802e29bf

[20] Nomura Y, Itoh H, Maed E, Masutani Y, Yoshikawa T, Hayashi N, *et al.* Shape based automated detection of pulmonary nodules with surface feature based false positive reduction. Int J CARS 2007; 2 (Suppl. 1): S355-S357.

[21] Koenderink JJ. Solid Shape. Cambridge, MA: MIT Press. 1990.

[22] Dorai C, Jain AK. COSMOS: a representation scheme for 3D free-form objects. IEEE Trans Pattern Anal Mach Intell. 1997 Oct; 19(10): 1115-30. http://dx.doi.org/10.1109/34.625113

[23] Lindeberg T. Scale-space theory in computer vision. Dordrecht, Netherlands: Kluwer Academic Publishers. 1994. http://dx.doi.org/10.1007/978-1-4757-6465-9

[24] Lorenz C, Carlsen IC, Buzug TM, Fassnacht C, Weese J. Multi-scale line segmentation with automatic estimation of width, contrast and tangential direction in 2D and 3D medical images. Lecture Notes in Computer Science. 1997 Mar; 1205: 233-42. http://dx.doi.org/10.1007/BFb0029242

[25] Sato Y, Nakajima S, Shiraga N, Atsumi H, Yoshida S, Koller T, *et al.* Three-dimensional multi-scale line filter for segmentation and visualization of curvilinear structures in medical images. Med Image Anal. 1998 Jun; 2(2): 143-68. http://dx.doi.org/10.1016/S1361-8415(98)80009-1

[26] Majer P. On the influence of scale selection on feature detection for the case of linelike structures. Int J Computer Vision. 2004 Dec; 60(3): 191-202. http://dx.doi.org/10.1023/B:VISI.0000036834.42685.b6

[27] Van Vliet LJ, Verbeek PW. Curvature and bending energy in digitized 2D and 3D images. Proceedings of the 8th Scandinavian Conference on Image Analysis. 1993: 1403-10.

[28] Beigelman-Aubry C, Raffy P, Yang W, Castellino RA, Grenier PA. Computer-aided detection of solid lung nodules on follow-up MDCT screening: evaluation of detection, tracking, and reading time. AJR Am J Roentgenol. 2007 Oct; 189(4): 948-55. PMid: 17885070. http://dx.doi.org/10.2214/AJR.07.2302

[29] Zhou J, Chang S, Metaxas DN, Zhao B, Schwartz LH, Ginsberg MS. Automatic detection and segmentation of ground glass opacity nodules. Lecture Notes in Computer Science. 2006 Oct; 4190: 784-91. http://dx.doi.org/10.1007/11866565_96

[30] Ikeda K, Awai K, Mori T, Kawanaka K, Yamashita Y, Nomori H. Differential diagnosis of ground-glass opacity nodules: CT number analysis by three-dimensional computerized quantification. Chest. 2007 Sep; 132(3): 984-90. PMid: 17573486. http://dx.doi.org/10.1378/chest.07-0793

フォーラム

治験開始前のサンプル検査データ提出における適切な同意取得方法の確立

山田奈央子* 玉見康江* 渡部歌織*
戸田智恵子* 青木敦* 河原崎秀一*
上田哲也* 山崎力* 荒川義弘*

Establishment of Standardized Procedures to Obtain Informed Consent for Submission of Sample Examination Data before Starting Trials

Naoko YAMADA, Yasue TAMAMI, Kaori WATANABE, Chieko TODA, Atsushi AOKI, Shuichi KAWARAZAKI, Tetsuya UEDA, Tsutomu YAMAZAKI and Yoshihiro ARAKAWA

Clinical Research Support Center, The University of Tokyo Hospital, Japan

An increasing number of clinical trials recently require the submission of examination data as sample to check the feasibility of the study before the trials are started. However, procedures to obtain informed consent have not been standardized. Therefore, we investigated various procedures by reviewing past cases and guidelines on research ethics and personal information protection. Based on this review, we developed the procedures for four types of study classified according to the prospective nature and degree of invasiveness of the examination. In type A, when the sample data is prospective and requires implementation of invasive examination not conducted as part of routine medical care, written informed consent is mandatory and each examination must be approved by the institutional review board (IRB). In type B, when the sample data is prospective and requires implementation of less invasive or non-invasive examination not conducted as part of routine medical care, use of pre-approved template of written informed consent that includes explanations of foreseeable risks and inconveniences accompanying the examination is required. In type C, when the sample data is prospective and uses results of examination conducted as part of routine medical care, informed consent can be obtained either orally or in writing at the discretion of the investigator. In type D, when the sample data uses preexisting medical data, efforts have to be made to obtain oral informed consent as far as possible. However, if informed consent is not possible, individual informed consent can be omitted but general notice should be given to patients regarding use of their medical records for purposes including answering inquires on medical services from other medical institutions. This classification system, which includes flowcharts and templates for informed consent, has been approved by the IRB at the University of Tokyo Hospital and will facilitate proper handling of sample data.

Key words: clinical trials, sample data, informed consent, ethical guidelines, privacy protection

Jpn J Clin Pharmacol Ther. 2015; 46(1): 21-27

1．背景・目的

近年，施設調査の一環として，検査を行う医療従事者の技能評価や適正なデータ解析の可否判定など，試験データの質を保証するために，試験開始前にサンプルとして検査データ（以下，サンプル検査データ）の提出が規定されている試験が増加してきている．提出するサンプル検査データはさまざまであり，すでに実施された検査で得られたデータで対応可能なものや，日常診療では行わない試験特有の手順どおりに実施することが求められることもある．

このサンプル検査データの提出は，研究の前段階として，検査の品質の確認のために行うもので，研究そのものではない．しかしながら，日常診療の外で研究に紐づいて実施するものであり，データの利用や侵襲的検査の実施については，協力者の同意や倫理的検討を要する行為であると考えられる．

そこで，本研究課題では既存の倫理指針等を参考に，既存資料であるか否かや侵襲的であるか否かにより分類し，そのうち，低侵襲の検査の場合や既存資料を利用する場合については，円滑かつ適切に進めるための同意取得方法について検討し，これらすべての手順について Institutional

* 東京大学医学部附属病院臨床研究支援センター
著者連絡先：山田奈央子 東京大学医学部附属病院臨床研究支援センター 〒113-8655 東京都文京区本郷7-3-1
E-mail：ymd-na@umin.ac.jp
投稿受付2014年9月2日，第2稿受付2014年10月27日，掲載決定2014年10月31日
ISSN 0388-1601